applied sciences

MDPI

Article

Enhancing the Photocatalytic Activity and Luminescent Properties of Rare-Earth-Doped CeO_2 Nanoparticles

Dana Toloman [1], Adriana Popa [1], Ramona Bianca Sonher [2], Rares Bortnic [2], Traian Florin Marinca [3], Ioana Perhaita [4], Miuța Filip [4,*] and Amalia Mesaros [2,*]

[1] National Institute for Research and Development of Isotopic and Molecular Technologies, 67-103 Donat Street, 400293 Cluj-Napoca, Romania; dana.toloman@itim-cj.ro (D.T.); adriana.popa@itim-cj.ro (A.P.)
[2] Physics and Chemistry Department, Technical University of Cluj-Napoca, 28 Memorandumului Street, 400114 Cluj-Napoca, Romania; ramona.mos@chem.utcluj.ro (R.B.S.); rares.bortnic@ubbcluj.ro (R.B.)
[3] Materials Science and Engineering Department, Technical University of Cluj-Napoca, 103-105 Muncii Avenue, 400641 Cluj-Napoca, Romania; traian.marinca@stm.utcluj.ro
[4] Raluca Ripan Institute for Research in Chemistry, Babes-Bolyai University, 30 Fântânele Street, 400294 Cluj-Napoca, Romania; ioana.perhaita@ubbcluj.ro
* Correspondence: miuta.filip@ubbcluj.ro (M.F.); amalia.mesaros@chem.utcluj.ro (A.M.)

Abstract: Our study is focused on the structural and morphological characteristics, optical behaviour and photocatalytic properties of undoped and 5 at% Eu^{3+}-, Gd^{3+}- and Y^{3+}-doped CeO_2 nanoparticles prepared by a green hybrid sol-gel combustion method. Several techniques such as X-ray diffraction powder (XRD), Transmission Electron Microscopy (TEM), UV-Vis spectroscopy, Photoluminescence spectroscopy (PL) and Electron Paramagnetic Resonance (EPR) have been used to investigate the obtained samples. Moreover, the correlation between the characteristics and properties has been studied. The nanoparticles observed by TEM exhibit a pseudo-spherical shape, except for Y^{3+}-doped CeO_2, which presents an acicular shape. The average size of undoped and rare-earth-doped CeO_2 nanoparticles is below 10 nm, in good agreement with the calculations performed based on XRD analyses. From UV-Vis analyses it has been deduced that with doping the band gap energy decreases, which shows that additional levels are introduced by doping into the CeO_2 band gap. The EPR spectra evidence similar behaviour for all doped samples. The photocatalytic activity was evaluated by the degradation of rhodamine B (RhB) under UV light irradiation. The photodegradation mechanism has been studied in depth based on the formation of electron-hole pairs, and to evidence the reactive oxygen species, ESR coupled with spin-trapping experiments was performed. In the case of Y-doped CeO_2 nanoparticles, the generation of both •OOH and $•O_2^-$ radicals involved in RhB photodegradation was highlighted.

Keywords: CeO_2 nanoparticles; rare-earth; photocatalytic activity; photoluminescence; ROS

Citation: Toloman, D.; Popa, A.; Sonher, R.B.; Bortnic, R.; Marinca, T.F.; Perhaita, I.; Filip, M.; Mesaros, A. Enhancing the Photocatalytic Activity and Luminescent Properties of Rare-Earth-Doped CeO_2 Nanoparticles. *Appl. Sci.* **2024**, *14*, 522. https://doi.org/10.3390/app14020522

Academic Editor: Edik U. Rafailov

Received: 30 November 2023
Revised: 3 January 2024
Accepted: 5 January 2024
Published: 7 January 2024

1. Introduction

Industrial progress has improved living standards, driving the development of human society. Therefore, some industrial pollutants are generated in wastewater effluents, such as heavy metals, radioactive nuclides, and organics [1]. Unfortunately, great amounts of wastewater are released into the environment, causing significant environmental pollution. Organic pollutants such as phenols, organic dyes and antibiotics are very toxic. These pollutants can be accumulated into aquatic organisms and from there along the food chain to the human body [2]. Thus, the discarding of organic pollutants represents one of the most important environmental problems. In recent years, many technologies have been employed in environmental remediation, including adsorption [3], biodegradation [4] and chemical oxidation [5]. The disadvantages of the above methods consist of the use of solvents and the generation of secondary metabolites which are very difficult to remove. One of the cost-effective methods that had been developed for the removal of organic

contaminants from wastewater is Advanced Oxidation Processes (AOPs). AOPs using semiconductor photocatalysts have been proven to be a promising technique for water disinfection due to its high efficiency, acceptable price, high stability and the capability to degrade organic pollutants and mineralization to CO_2 and H_2O as the final products [6].

The efficiency of the photocatalytic process depends on the operational parameters that dominate the adsorption and photodegradation of dye molecules. Among these parameters, the most important are the initial pH of the dye solution, the concentration of the photocatalyst and dye, the reaction temperature and the dopants content [6,7]. Tirumala et al. show that controlling the incident light intensity and wavelength is a mode for controlling and tuning the activity and selectivity of the catalyst [8]. Also, in a doped semiconductor photocatalyst, the positively or negatively charged microenvironment around trapped holes or electrons influences the ability of photocatalyst to generate reactive oxygen species (ROS) involved in reactions of photo-oxidation and photo-reduction [9,10].

A great number of semiconductor metal oxides, such as TiO_2 [11], ZnO [12], SnO_2 [13], etc., have been used as photocatalytic materials. As one of the most popular metal oxide semiconductors, the rare earth oxide ceria (CeO_2) is extensively used in many fields due to its ability to extract, store and release oxygen. Its applicative potential based on this special feature includes domains like catalysis, photocatalysis, solid oxide fuel cells, ceramics, sunscreens, solar cells, gas sensors and biomedical areas such as biosensing, bioimaging or targeted drug therapy, etc. [14–19]. Moreover, ceria has proved to be an ideal candidate as an artificial oxygen modulator, and this is vital for many biological processes [20]. Also, nanoceria is well-known for its enhanced catalytic reactivity due to easy conversion between cerium's tetravalent and trivalent valence surface states [21]. In ceria, the tetravalent cerium ion, Ce^{4+}, transforms into a trivalent state, Ce^{3+}, and this transformation produces a good yield of oxygen vacancies without changes in the chemical environment [22]. Additionally, it is nontoxic, abundant and absorbs light in the near UV and also marginally in the visible region, properties which can be used in heterogeneous photocatalysis [23]. Thus, the application of CeO_2 is obstructed. Many strategies have been used to enhance the catalytic/photocatalytic activity by tuning the structural and morphological characteristics [24]. One strategy to extend the utilization of visible light over CeO_2 consists of suitable doping with various metal ions: isovalent cations (Ti^{4+}, Zr^{4+}, Hf^{4+}, Sn^{4+}, etc.) or aliovalent cations (Mn^{2+}, Zn^{2+}, Ca^{2+}, La^{3+}, Eu^{3+}, Sm^{3+}, Y^{3+}, Eu^{3+}, Mn^{3+}, Sc^{3+}, Gd^{3+}, Sm^{3+}, etc.) [25]. It has been demonstrated theoretically and experimentally that the substitution of cerium ions with isovalent dopant cations induces a decrease in oxygen vacancy formation energy due to the structural distortion, whereas in the case of aliovalent dopants the generation of extra oxygen vacancies into the ceria lattice has been evidenced due to the synergism between the structural distortion and electron modifications [25–27]. On the other hand, the trivalent cations of rare earth metals drastically modify the reactivity structure and optical emission of ceria [21,28–30]. The luminescent properties of undoped or rare earth (Eu^{3+}, Sm^{3+}, or Tb^{3+})-doped ceria have been reported and the emission mechanism proposed by considering the transfer of the charge carrier between the Ce 4*f* conduction band and the O 2*p* valence band. Also, the broad photoluminescence emission in the visible domain is attributed to defects, including oxygen vacancies in the ceria lattice with electronic energy levels below the 4*f* band [31–33].

To date, a lot of chemical strategies have been developed to synthesize undoped or doped ceria nanoparticles, such as solid-state reactions [34], co-precipitation [35], hydrothermal techniques [36], sol-gel [37], microwave-assisted synthesis [38], ultrasonic spray pyrolysis [39], sonochemical synthesis [40], combustion method [41] and so on, proving that the physical and chemical properties are strongly dependent on the synthetic route used. In this regard, Amoresi et al. studied the correlation between a wide range of CeO_2 morphologies, such as nanorods, nanocubes, nanobeans and nanohexagons and the photocatalytic activity [42]. A similar study has been published by Ortega et al. with emphasis on the Eu-doped ceria nanostructures [43]. It has been demonstrated that enhanced photocatalytic performance is obtained by increasing the charge carrier concentration and light absorption

capacity by defects induced by the dopants into CeO_2 nanostructures. Nevertheless, studies are still ongoing for a deeper understanding of the correlations between the experimental parameters, structure, morphology, luminescence properties and photocatalytic activity.

Considering the previous research works reported in the literature, this paper focuses on the effects induced by the incorporation into the ceria lattice of Eu^{3+}, Gd^{3+} and Y^{3+} aliovalent cations by studying the correlations between the structural and morphological characteristics and luminescence properties and photocatalytic activity. These materials have been synthesized by a green hybrid sol-gel combustion method and characterized by using various techniques, namely X-ray Diffraction, Transmission Electron Microscopy, UV-Vis spectroscopy, Photoluminescence (PL) and Electron Paramagnetic Resonance (EPR). Finally, we attempt to provide an overview of how the selected rare earth ions influence the ceria's structure, morphology and photocatalytic activity.

2. Materials and Methods

2.1. Materials

Commercial ammonium cerium (IV) nitrate, $(NH_4)_2Ce(NO_3)_6$, (Merck, 98.5%), gadolinium nitrate hexahydrate, $Gd(NO_3)_3{\cdot}6H_2O$ (99.9%, Merck), europium acetate hydrate $Eu(CH_3\text{-}COO)_3{\cdot}xH_2O$ (99.9%, Merck), yttrium acetate hydrate $Y(CH_3\text{-}COO)_3{\cdot}xH_2O$ (99.9%, Merck), sucrose, $C_{12}H_{22}O_{11}$ (99.5%, Sigma-Aldrich), pectin from citrus peel, (Sigma-Aldrich), rhodamine B (RhB), $C_{28}H_{31}ClN_2O_3$ (analytical standard, Merck), acetonitrile, C_2H_3N (ACN, HPLC-grade, Merck) and ortho-phosphoric acid (H_3PO_4, 85%, Merck) were used without any further purification.

2.2. Nanoparticle Synthesis

The undoped and Eu^{3+}-, Gd^{3+}- and Y^{3+}-doped CeO_2 nanoparticles were synthetized via a green hybrid sol-gel combustion method developed by Goga et al. [44] using sucrose as a poly-condensation agent and pectin as a chelation agent. Briefly, the corresponding amounts of metal salts—for the doped systems 5 at% of Eu^{3+}, Gd^{3+} and Y^{3+} ions relative to CeO_2—were dissolved in MiliQ water (0.05 M) at 60 °C for an hour under vigorous magnetic stirring. Similarly, a sucrose solution (0.1 M) was prepared using milli-Q water, at 60 °C, under magnetic stirring. The two solutions were mixed in the presence of the pectin (the sucrose to pectin weight ratio was 1:5). The pH value was monitored during the synthesis and no correction was necessary to maintain an acidic medium in the solution. The pH value of the final solutions was determined to be in the range of 1.5–2. The as-obtained mixture was dried in air, on the sand bath. At 215 °C, a spontaneous combustion of the synthesis mixture was observed and a dispersed yellow powder was obtained. The evolved gases were captured and absorbed in a soda lime aqueous solution. The following chemical reaction can be considered in the formation of ceria nanoparticles:

$$(1-x)Ce^{3+} + xRE^{3+} + 2NH_4{}^{+} + 6NO_3{}^{-} + 2C_{12}H_{22}O_{11} + 26O_2 \rightarrow Ce_{(1-x)}RE_xO_2 + 24CO_2\uparrow + 26H_2O + 8NO_2\uparrow$$

The use of non-toxic reagents such as sucrose and pectin give the process a green synthesis approach, but the reaction is not an environmentally friendly reaction due to the production of nitrogen dioxide.

2.3. Characterization Techniques

The structural characterisation of the obtained nanoparticles was undertaken through X-ray diffraction (XRD). The equipment used was an INEL Equinox 3000 diffractometer, which works in reflection mode, and it is equipped with a curved multidetector. The wavelength used was the one characteristic of Co, Kα radiation (λ = 1.7903 Å). The mean crystallite size was calculated with the Scherrer method [45]. The lattice parameter was calculated using Celref version 3 refinement software [46]. TEM images were obtained by scanning transmission electron microscopy (STEM) using a Hitachi HD2700 Electron Microscope (Hitachi, Tokyo, Japan). Absorption spectra were recorded using a JASCO

V570 UV–VIS-NIR Spectrophotometer equipped with an absolute reflectivity measurement JASCO ARN-475 accessory. Luminescent characteristics of samples were evaluated based on emission spectra registered with a Wavell JASCO FP-6500 spectrofluorimeter, equipped with a PMT R928 photomultiplier (glass filter UG1—Reichmann Feinoptik, GER). Electron paramagnetic resonance (EPR) spectroscopy measurements of powder samples were carried out using a Bruker E-500 ELEXSYS spectrometer (Karlsruhe, Germany) at room temperature under identical conditions: The measurements were conducted at Xband (9.52 GHz) microwave power 2 mW, with a modulation frequency of 100 kHz. To determine the reactive oxygen species (ROS) generation, the EPR spectrometer coupled with the spin trapping probe technique was used. As the spin trapping reagent, DMPO was used. The nanoparticles (10 mg) were dispersed in DMSO (1 mL) and homogenized in an ultrasound bath (30 min) before use. DMPO of 0.2 mol/L concentration was added to the solution. The obtained solution was subjected to visible irradiation for 25 min and immediately before measurement transferred into the quartz flat cell, optimized for liquid measurements. The photodegradation of Rhodamine B (RhB) was carried out in a Laboratory-Visible-Reactor system using a 400 W halogen lamp (Osram) [47]. The catalyst (5 mg) was suspended in an aqueous solution of RhB (1.0×10^{-5} mol·L^{-1}, 10 mL) and then the mixture was stirred in the dark to achieve the adsorption equilibrium on the catalyst surface. Each degradation experiment was continuously conducted for 6 h. The mixture (3.5 mL) was withdrawn for analysis every 60 min. After separating the catalyst from the suspensions by centrifugation, the solution was analysed by the UV–Vis spectrophotometer by recording the maximum absorbance of RhB at 554 nm.

RhB removal rate is calculated using the following equation:

$$\text{Removal rate} = \frac{A_0 - A_t}{A_0} \times 100$$

where A_0 and A_t represent the RhB absorbance initially and at time t, respectively.

The HPLC analyses were performed on a Jasco HPLC chromatograph (Jasco International Co., Ltd., Tokyo, Japan) that was equipped with an intelligent pump, PU-980, a ternary gradient unit, LG-980-02, an intelligent column thermostat, CO-2060 Plus, an intelligent detector, UV-975, an intelligent fluorescence detector, FP-2020 Plus, and an injection valve that was equipped with a 20 µL sample loop (Rheodyne, Thermo Fischer Scientific, Waltham, MA, USA). The system was controlled, and the experimental data processed with the ChromPass software (version v1.7, Jasco International Co., Ltd., Tokyo, Japan). Separation was performed on a Gemini chromatographic column (5µ C18, 110 Å, 250 × 4.6 mm, Phenomenex, Torrance, CA, USA) at 21 °C. Isocratic elution was performed with 45% of acetonitrile with 55% of 0.1% H_3PO_4 buffer. The flow rate was 1 mL/min and the injection volume was set to 20 µL. UV detection was performed by fluorescence at the excitation and emission wavelengths set at 535 nm and 580 nm. All the experiments were performed in triplicate. The determination of rhodamine B was performed according to the adapted method described by Chiang et al. [48].

3. Results and Discussion

The structural characteristics of undoped or RE-doped CeO_2 samples were determined by X-ray diffraction measurements and the corresponding diffraction patterns are shown in Figure 1. All diffraction lines are well indexed to the face-centred cubic (*fcc*) fluorite structure of CeO_2 (JCDD PDF 034-0394). No peaks belonging to any other phase have been observed in the XRD patterns, indicating the high structural purity of the samples. The effects of the dopant on the lattice parameters and crystallite sizes—calculated using the Scherrer method—are presented in Table 1.

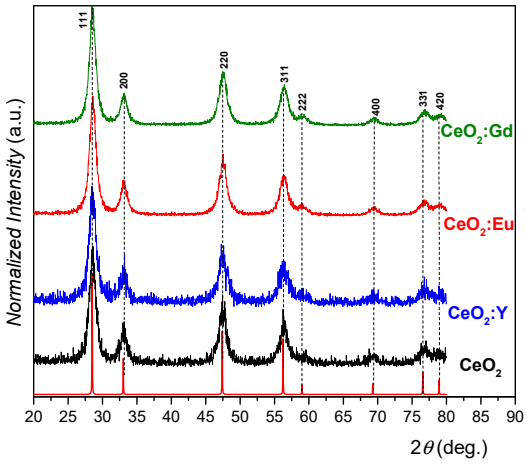

Figure 1. X-ray diffraction patterns of pure ceria, CeO_2; Y-doped CeO_2, CeO_2:Y; Eu-doped ceria, CeO_2:Eu; and Gd-doped ceria, CeO_2:Gd. All reflections have been indexed according to the JCDD PDF 034-0394 for CeO_2 face-centred cubic fluorite structure.

Table 1. Average crystallite sizes (D) and lattice parameters (a) of undoped and doped ceria.

Sample	Crystallite Size D (nm) [a]	Lattice Parameter a (Å) [a]	Energy Band Gap Eg (eV)
Undoped CeO_2	8.16	5.4105	2.98
CeO_2:Eu	8.40	5.4130	2.93
CeO_2:Gd	8.40	5.4129	2.88
CeO_2:Y	7.79	5.4113	2.93

[a] Calculates from XRD.

It has been demonstrated that the substitution of Ce^{4+} ions with a larger ion radius dopant cation alters the local chemistry and induces an enlargement of the crystal lattice due to steric effects [49–51]. The substitution into the ceria lattice of octahedral Ce^{4+} ions (Ce^{4+} = 0.97 Å) with a larger sized dopant (Gd^{3+} = 1.053 Å; Eu^{3+} = 1.066 Å and Y^{3+} = 1.019 A [52]) induced a slight increase in the lattice parameter values. Regarding the crystallite sizes it can be noted that the small amount of dopant ions stimulates the nucleation and the growth processes of the nanocrystals. This tendency can be noticed for the crystallite sizes in the cases of Gd^{3+} and Eu^{3+}. The introduction of Y^{3+} into the ceria lattice led to a diminishing of the crystallite size.

The morphological characterization of the samples has been achieved via TEM investigations—Figure 2. TEM images show the formation of pseudo-spherical nanoparticles with a high tendency to agglomerate. Analysis of these images disclosed that the particle sizes are below 10 nm, which is in good concurrence with the XRD results. This means that each particle is composed of only one crystallite. In the case of the Y-doped ceria sample, the presence of some aggregates with an acicular shape should be noticed. The changing of nanoparticles' shapes by introducing different types of dopants indicate that the crystallisation process can be tailored.

The absorption spectrum of nanoparticles in the UV-Vis-NIR domain is affected by various factors such as optical band gap, oxygen vacancies, the presence of an impurity centre, etc. Figure 3a shows the absorbance spectra of pure and RE-doped ceria nanostructures and the spectra exhibit a strong absorbance in the UV region. In general, the absorption band below 400 nm is assigned to the transitions of charge transfer between O 2*p* and Ce 4*f* orbitals in cerium oxide [53]. Doping with RE caused a red shift in the absorbance band of ceria, indicating that 4*f* or 4*d* transition metals ions induce intermediate electronic energy levels between the O 2*p* and Ce 4*f* orbitals of cerium oxide [54]. To evaluate the energy band gap of the samples, Tauc's relation was applied to the absorption spectra. Figure 3b displays the Tauc plots. The energy band gaps of RE-doped CeO_2 nanoparticles are smaller

than those corresponding to ceria (2.98 eV)—Table 1. The band gap narrowing of CeO_2 by doping with RE ions can be explain by the formation of 4*f* for Gd and Eu or 4*d* for Y states below the conduction band edge, which extend the absorption of ceria into the visible region.

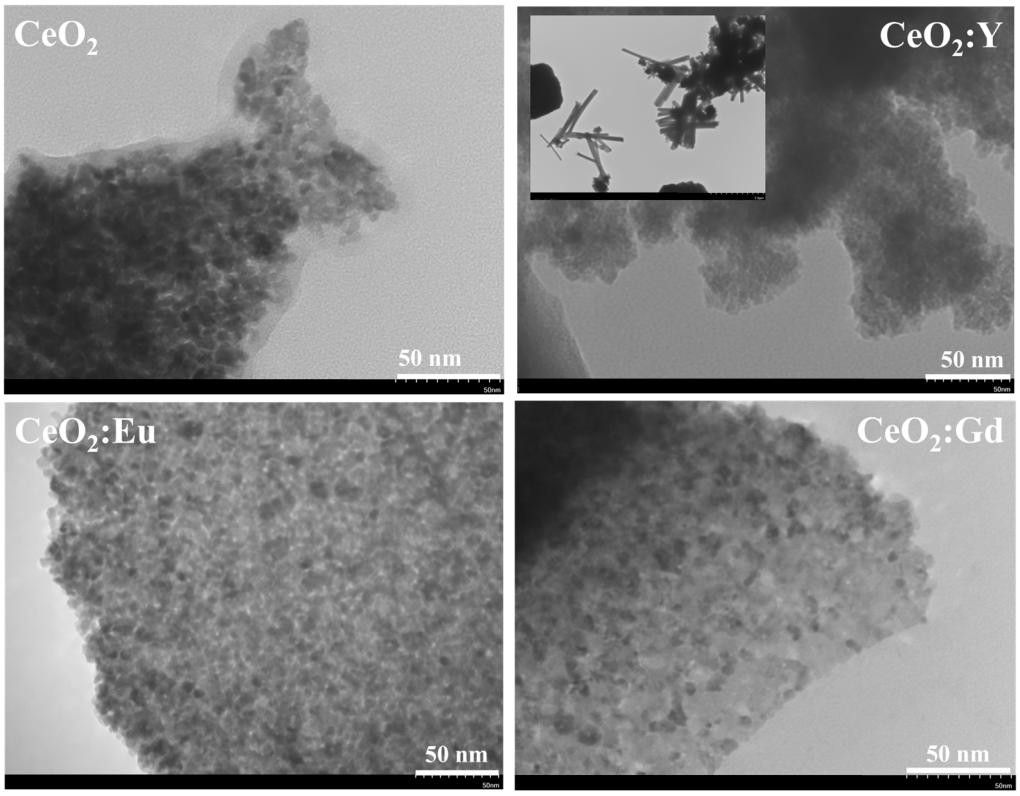

Figure 2. TEM images of undoped ceria, CeO_2; Y-doped CeO_2, CeO_2:Y; Eu-doped ceria, CeO_2:Eu; and Gd-doped ceria, CeO_2:Gd. The scale bar is 50 nm for all images, except the inset of CeO_2:Y; here, the scale bar is 2 μm.

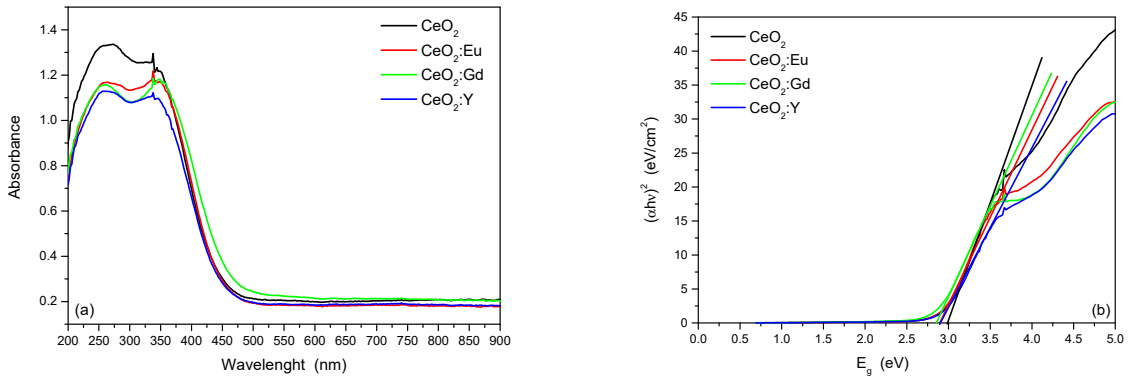

Figure 3. (**a**) Room temperature optical absorption spectra and (**b**) Tauc plots of undoped and RE doped ceria nanoparticles.

Photoluminescence spectroscopy is considered an important technique for understanding the role of the recombination of electron pairs and defects in modifying the photocatalytic activity of a material. The registered spectra for the ceria-based samples are presented in Figure 4. The literature data reported that the energy of emitted photons due to the electron transitions from the 4*f* band to the valence band in CeO_2 lies in the range of 3.0–3.8 eV [21]. The band centred at 364 nm, presented in all spectra, should be attributed to this transition. Also, it is reported that the emission bands located from 400 to

500 nm are attributed to some defects, such as vacancies or dislocations in CeO_2 [21,55]. Therefore, the conclusive transitions from Ce 4*f* level to O 2*p* level due to abundant defects like O vacancies and dislocations are responsible for emission peaks from the 430 nm to 494 nm domains observed in all spectra. The replacement of Ce^{4+} cations by RE^{3+} cations in the lattice of CeO_2 generates the formation of defects and oxygen vacancies in order to preserve the charge balance.

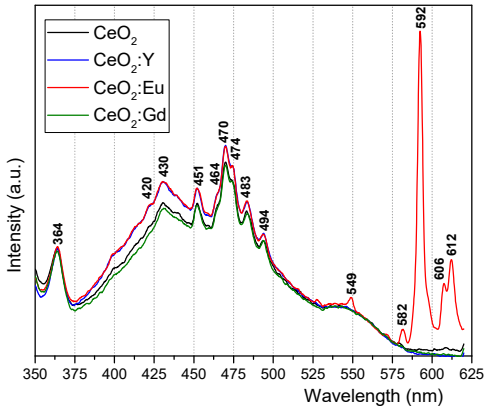

Figure 4. The room temperature photoluminescence spectra of undoped and RE-doped CeO_2 (λ_{exc} = 325 nm).

The photoluminescence spectrum of Eu-doped ceria is significantly different from the other registered spectra, showing well-defined emission bands in the 540–620 region. These bands result directly from the incorporation of the Eu^{3+} ions into the CeO_2 lattice. Depending on the excitation wavelength, possible f-f transitions of Eu^{3+} cations ($^5D_0 \rightarrow {}^7F_J$) take place at 550 nm (J = 0), 593 nm (J = 1), 610–630 nm (J = 2), 650 nm (J = 3), and 710 nm (J = 4) [56]. It is already known that the Ce site in the fluorite CeO_2 lattice presents Oh symmetry with eightfold oxygen coordination. Therefore, the Ce site possesses inversion symmetry and the electric dipole emission $^5D_0 \rightarrow {}^7F_2$ could be forbidden and could not be observed only if the Eu^{3+} ion occupied the Ce site without changing the original inversion symmetry. When Eu^{3+} replaces Ce^{4+}, it needs charge compensation in order to obtain a charge equilibrium. Two kinds of defects could be formed during charge compensation: * interstitial Eu^{3+} (four Eu^{3+} replacing three Ce^{4+}) and **O^{2-} vacancies (one Eu_2O_3 replacing two CeO_2). These defects induce the symmetry distortion of the local environment around the Eu^{3+} ions. Moreover, due to the difference in ionic radius between Ce^{4+} and Eu^{3+}, the replacement of Ce^{4+} ions with Eu^{3+} ions also generates the symmetry distortion of the local environment around the Eu^{3+} ions [56].

The presence in the spectrum (λ_{exc} = 325 nm) of $^5D_0 \rightarrow {}^7F_0$ transition, around 549 nm, $^5D_0 \rightarrow {}^7F_1$ transition at 592 nm and $^5D_0 \rightarrow {}^7F_2$ at 606 and 612 nm, respectively, suggests that Eu^{3+} cations replace Ce^{4+} sites in the CeO_2 lattice and moreover is indicative of the formation of oxygen vacancies [57–60].

To evidence the presence of paramagnetic species, the EPR technique was used. The spectra were similar, and as an example the experimental spectrum of CeO_2-Y nanoparticles obtained at room temperature is illustrated in Figure 5a. The spectrum shows a signal at a higher value than the free spin value (g_e = 2.0023), and two signals at lower g values. The EPR signal at g = 2.00935 was assigned to physisorbed oxygen molecules or to paramagnetic species such as $\bullet O_2^-$ generated from these oxygen molecules [61], and that centred g = 1.964 has been attributed both to quasi-free electrons and to Ce^{3+} ions [62]. Both paramagnetic impurities are due to the non-complete stoichiometry obtained during the synthesis process.

The effect of the charge separation in semiconducting oxides under irradiation can be probed by EPR. Therefore, the CeO_2-Y sample was irradiated with UV to check the modification of the spectrum (Figure 5a). Under irradiation, only the resonance signal centred at g = 2.00935 changes its intensity. This behaviour can be explained by the

following: when CeO_2 is irradiated with photons owing energy higher than that of the band gap, electron–hole pairs are generated. If these pairs do not recombine, the electrons are stabilized on cations, while the holes are stabilized by oxygen anions [63]. Thus, the photoexcited electrons are stabilized by Ce^{4+} ions, being reduced to Ce^{3+}; the increases of the resonance signal attributed to this signal are not visible because of the high value of spin orbit coupling and therefore the very fast relaxation time [64].

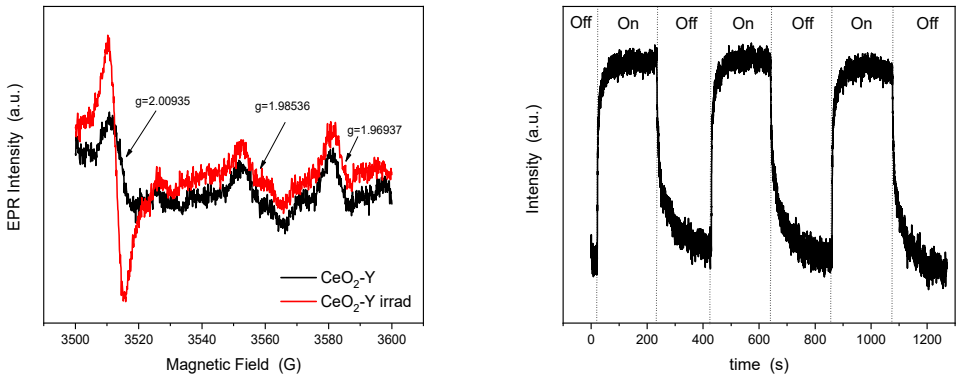

(**a**) (**b**)

Figure 5. (**a**) EPR spectra of CeO_2-Y nanoparticles obtained without and under UV irradiation. (**b**) Monitorization of $\bullet O_2^-$ signal under UV irradiation in three on-off cycles.

To illustrate the charge generation and recombination, the intensity of the EPR signal centred at g = 2.00935 was monitored under UV irradiation in three on–off cycles. The obtained kinetic is exhibited in Figure 5b. It can be observed that when the UV is turned on, the EPR signal increased faster and charge carriers stayed at the excited energy level; after turning off the light, the signal decreased, but a little slowly, which means that the recombination process is longer. The on–off cycle experiments show that the process is reversible.

The photocatalytic activity of the samples was investigated against Rhodamine B (RhB) solution under visible irradiation. Prior to the photocatalytic experiments, the samples dispersed in solution were kept for 60 min in the dark to achieve an adsorption–desorption equilibrium. The RhB removal rate was monitored by the temporal evolution of RhB absorbance. As an example, Figure 6 shows the evolution in time after dark adsorption and the visible irradiation of RhB absorbance in the presence of the CeO_2-Gd sample. It could be observed that the RhB absorbance decreases with irradiation time. The decrease in the absorption peak is due to the cleavage of the RhB chromophore ring structure, and the shift of the absorption maximum results in the N-deethylation of RhB molecules [65].

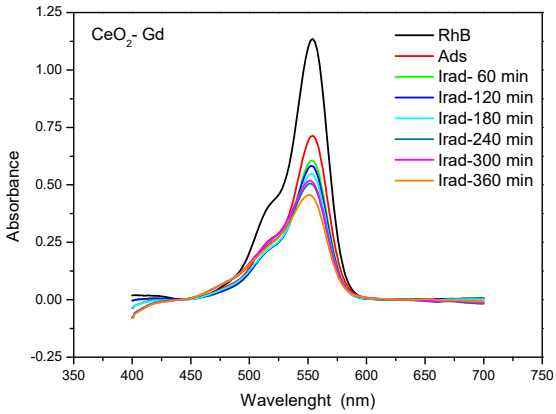

Figure 6. Evolution in time of RhB absorbance after dark adsorption and visible irradiation in the presence of CeO_2-Gd sample.

The RhB removal rate in the presence of all the samples is depicted in Figure 7. All doped samples possess enhanced adsorption capacity relative to ceria nanoparticles. Figure S2 shows the adsorption capacity of Y dopedCeO_2 sample for 420 min which proves that after 60 min, the adsorption equilibrium was reached. The enhanced dark adsorption capacity of doped samples could be due to much more active sites for the dye molecules to react. The removal rate of the CeO_2-Gd sample is almost three times higher than that corresponding to ceria.

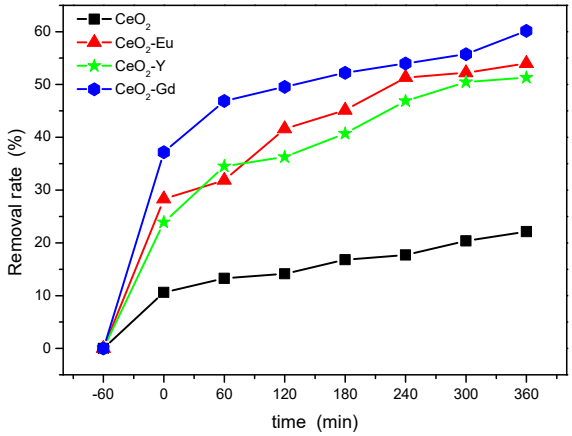

Figure 7. Removal rate of RhB solution in the presence of each sample.

The photocatalytic process could be described by the first order kinetic model following the equation

$$-ln\frac{A_t}{A_0^*} = k_i \cdot t$$

where A_t—absorbance of RhB at t time; A_0^*—absorbance of RhB after dark adsorption; t—irradiation time; and k_i—apparent kinetic constant. The obtained plots show a linear relationship with the irradiation time (Figure 8). In Table 2 are shown the calculated rate constants and correlation coefficients corresponding to Figure 8. From the obtained k values, it can be seen that the best performance was obtained using Y-CeO_2, followed by Eu-CeO_2 > Gd-CeO_2 > CeO_2.

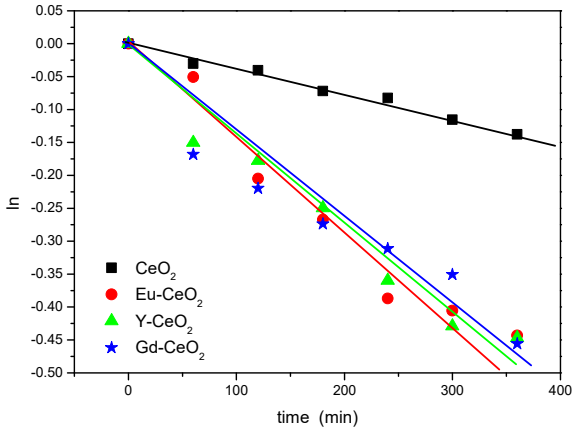

Figure 8. Evaluation of photodegradation kinetic.

The photocatalytic mechanism can be explained based on the formation of electron–hole pairs. Under visible irradiation, electrons absorb energy and move from the valence band to the conduction band, resulting in the appearance of electron–hole pairs. The electrons interact with oxygen and produce superoxide radicals and the holes interact with H_2O, resulting in hydroxyl radicals. These radicals are known as radical oxygen species and are capable of degrading organic pollutants. The photocatalytic activity depends on

the capacity of the photocatalyst to separate the electron–hole pairs. The most important factor is represented by the rate of electron–hole pair separation and recombination. The delay in recombination drives enhanced photocatalytic activity [24].

Table 2. The apparent first-order rate constant k of photocatalytic degradation and correlation coefficient, R^2.

Sample	$K \times 10^{-3}$	R^2
CeO_2	0.37	0.9860
CeO_2:Eu	1.13	0.9441
CeO_2:Gd	1.09	0.9244
CeO_2:Y	1.24	0.9594

To evidence the reactive oxygen species, ESR coupled with spin-trapping experiments was performed. The experimental spectrum is shown in Figure 9. The obtained spectrum is a complex one, consisting of many resonance lines which are due to several species. To identify the species, a simulation of the spectrum was carried out. The simulated spectrum is also shown in Figure 9 and was obtained through a linear combination of the following spin adducts: •DMPO–OCH_3 (a_N = 13.3 G, a_H^β = 8.3 G, a_H^γ = 1.9 G, relative concentration 60%), •DMPO–O_2^- (a_N = 12.9 G, a_H^β = 11.4 G, a_H^γ = 2.6 G, relative concentration 31%) and nitroxide-like radicals (a_N = 13.9 G, relative concentration 9%).

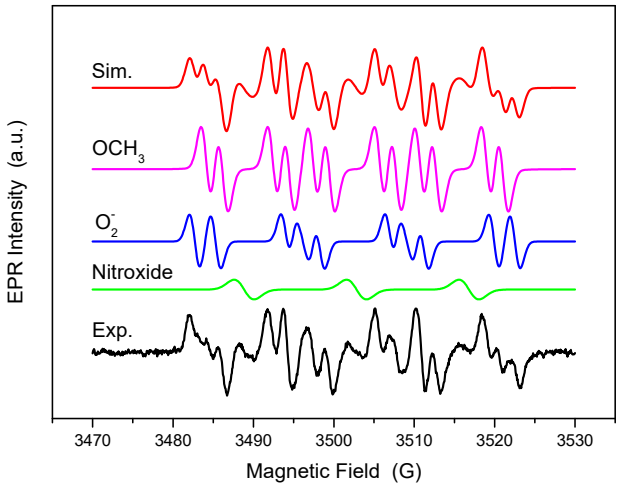

Figure 9. Experimental and simulated spectra of DMPO spin adducts generated by Y-CeO_2 photocatalyst suspension in DMSO after 25 min visible irradiation.

The proof of the •OH radical existence in the system is due to the presence of •DMPO–OCH_3 spin adducts, since these spin adducts are generated by the reaction between •OH radicals and DMSO solvent [66]. Nitroxide-like radicals were generated by the cleavage of the NAC bond followed by the ring opening of DMPO [67].

The roles of scavengers in elucidating the active radical species involved in photodegradation are to capture and suppress the action of the species under investigation during the photocatalytic process. The scavenger experiment was performed to evaluate the active radical species that participated in the photocatalytic process. Ethylenediaminetetraacetic acid (EDTA) and vitamin C (Vit C) were used as h^+ and •O_2^- radical scavengers, respectively [68]. The scavenger experimental conditions were the same as those used for the RhB degradation and 1.0 mM scavenger was added to the solution. In Figure 10, all samples showed lower RhB degradation than the control experiment (with no scavenger), which attested that these radical species are involved in the photocatalytic process. The dominant active species showed the weakest photocatalytic activity. Therefore, the lowest

RhB degradation was obtained with Vit C, indicating that $\bullet O_2^-$ radicals are the main species involved in RhB photodegradation.

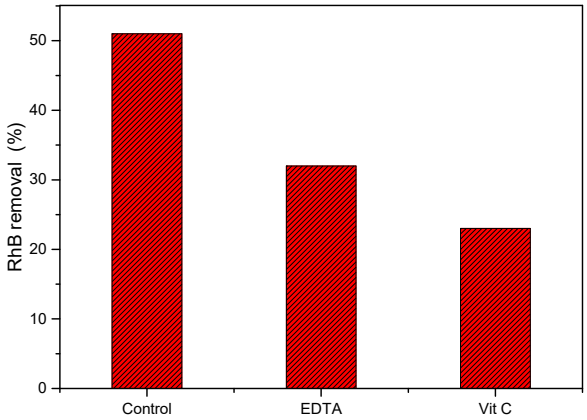

Figure 10. Scavenger experiment results of Y-CeO_2 nanoparticles for RhB degradation (control experiment = no scavenger).

Based on the above studies, the photocatalytic mechanisms of Y-, Gd- and Eu-doped CeO_2 nanoparticles are illustrated in Figure 11. The doping of CeO_2 results in a higher concentration of oxygen vacancies and additional doping transition levels. When the doped CeO_2 is irradiated with visible light, the photogenerated electrons will move in the conduction band and the holes will be generated in the valence band. Part of the electrons will be trapped on the doping levels, limiting the recombination of the photoinduced electron and hole pairs [69]. Therefore, the electrons from the conduction band will interact with oxygen-producing superoxide radicals and the holes will interact with H_2O, generating hydroxyl radicals. Both generated radical species will participate in a redox reaction, being capable of degrading the RhB molecule. From scavenger experiments it can be found that $\bullet O_2^-$ radicals are the main species required to degrade RhB dye; indeed, $\bullet O_2^-$ radicals are generated by the sample, but hydroxyl radicals are the majority, which explains the not-very-high photocatalytic performances of the samples.

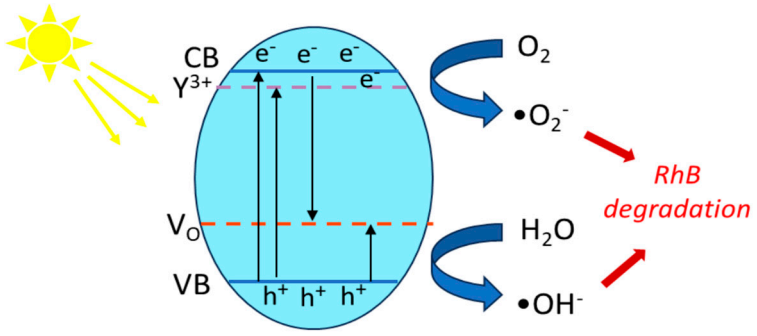

Figure 11. Degradation mechanism of Y-doped CeO_2 nanoparticles.

The HPLC method has been used as a complementary method to determine the concentration in RhB of the solutions formed after the UV photodegradation process. The obtained concentration values for all samples are summarized in Table 3 and the chromatograms are presented in Figure S1—Supplementary Material.

Table 3. HPLC-FD concentrations of RhB before and after photodegradation with CeO_2-doped catalysts (CeO_2:Eu; CeO_2:Gd; CeO_2:Y).

Catalyst	No Catalyst	CeO_2	CeO_2:Eu	CeO_2:Y	CeO_2:Gd
Rhodamine B [mg/L]	4.640	2.440	1.386	0.700	0.430

The obtained results suggest a decreasing tendency for RhB concentration after the photodegradation of the pollutant solution with CeO_2-doped catalysts (CeO_2 > CeO_2:Eu > CeO_2:Y > CeO_2:Gd), sustaining the previous results obtained using UV–Vis spectroscopy.

4. Conclusions

In summary, CeO_2 nanoparticles doped with rare earth ions (Eu^{3+}, Gd^{3+} and Y^{3+}) were synthetized via a green hybrid sol-gel combustion method. The nanoparticles have a face-centred cubic (*fcc*) fluorite structure, and the slight increase in the cell parameters sustains the replacement of Ce^{4+} with dopant ions. Undoped CeO_2 has a small crystallite size (around 8 nm) and by doping a slight increase was noticed, except for Y ions. The particle size evaluated by TEM is in accordance with the crystallite size evaluated by XRD, sustaining the formation of monocrystalline particles. By doping the band gap, the energy decreases, which shows that additional levels are introduced by doping into the CeO_2 band gap. The EPR spectra evidence similar behaviour for all doped samples. The intense signal at g~2.0093 was assigned to physisorbed oxygen molecules or to paramagnetic species such as $\bullet O_2^-$ generated from these oxygen molecules, and a lower one at g~1.964 was due to quasi-free electrons or Ce^{3+} ions. Under UV light irradiation, the signal at g~2.0093 increases in intensity, which suggests an efficient charge separation by capturing the photogenerated holes with oxygen anions. The charge generation and recombination processes are reversible. The RhB removal rate was tested under UV light irradiation. The removal of pollutant molecules is due to two processes, adsorption and photocatalysis. The best performance was obtained using Gd-CeO_2, with the adsorption playing an important role. But the best photocatalytic activity was obtained for Y-doped CeO_2. The spin-trapping experiment revealed the generation by Y-CeO_2 nanoparticles of both •OOH and $\bullet O_2^-$ radicals involved in RhB photodegradation. In our future works, studies of the photocatalytic degradation of other organic pollutants will be considered.

Supplementary Materials: The following supporting information can be downloaded at: https://www.mdpi.com/article/10.3390/app14020522/s1, Figure S1: HPLC chromatograms of RhB for the initial solution—a; undoped CeO_2—b; Eu-doped CeO_2—c; Y-doped CeO_2—d; Gd-doped CeO_2—e; Figure S2: The dark adsorption capacity of CeO_2-Y sample for 420 min.

Author Contributions: Conceptualization, D.T. and A.M.; methodology, D.T., A.P., R.B. and A.M.; investigation, D.T., A.P., R.B.S., R.B., T.F.M., I.P. and M.F.; writing—original draft preparation, D.T. and A.M.; writing—review and editing, D.T., A.P., R.B.S., T.F.M., I.P., M.F. and A.M.; visualization, D.T., A.P. and A.M.; supervision, M.F. and A.M.; project administration, A.M. All authors have read and agreed to the published version of the manuscript.

Funding: Financial support was provided by a grant from the Ministry of Research, Innovation and Digitalization, CNCS—UEFISCDI, project number PN-III-P4-PCE-2021-1561, and from the MCID through the "Nucleu" Programe within the National Plan for Research, Development and Innovation 2022–2027, project PN 23 24 01 03.

Institutional Review Board Statement: Not applicable.

Informed Consent Statement: Not applicable.

Data Availability Statement: The data presented in this study are available on request from the corresponding author.

Conflicts of Interest: The authors declare no conflicts of interest.

References

1. Shah, M.P. Chemistry in the Environment. In *Biological Treatment of Industrial Wastewater*; The Royal Society of Chemistry: London, UK, 2021; pp. 1–11, ISBN 978-1-83916-539-9.
2. Wang, C.C.; Li, J.R.; Lv, X.L.; Zhang, Y.Q.; Guo, G. Photocatalytic organic pollutants degradation in metal–organic frameworks. *Energy Environ. Sci.* **2014**, *7*, 2831–2867. [CrossRef]
3. Ali, I.; Gupta, V.K. Advances in water treatment by adsorption technology. *Nat. Protoc.* **2006**, *1*, 2661–2667. [CrossRef] [PubMed]

4. Kagle, J.; Porter, A.W.; Murdoch, R.W.; Rivera-Cancel, G.; Hay, A.G. Biodegradation of pharmaceutical and personal care products. *Adv. Appl. Microbiol.* **2009**, *67*, 65–108. [CrossRef] [PubMed]
5. Wenk, J.; Aeschbacher, M.; Salhi, E.; Canonica, S.; von Gunten, U.; Sander, M. Chemical Oxidation of Dissolved Organic Matter by Chlorine Dioxide, Chlorine, And Ozone: Effects on its optical and antioxidant properties. *Environ. Sci. Technol.* **2013**, *47*, 11147–11156. [CrossRef] [PubMed]
6. Hejazi, R.; Mahjoub, A.R.; Khavar, A.H.C.; Khazaee, Z. Novel visible-light-responsive rGO-ZnO@Bi_2MoO_6 nanocomposite with enhanced light harvesting and Z-scheme charge transfer for photodegradation and detoxification of RhB. *Solid State Sci.* **2019**, *95*, 105934. [CrossRef]
7. Rafiq, A.; Ikram, M.; Ali, S.; Niaz, F.; Khan, M.; Khan, Q.; Maqbool, M. Photocatalytic degradation of dyes using semiconductor photocatalysts to clean industrial water pollution. *J. Ind. Eng. Chem.* **2021**, *97*, 111–128. [CrossRef]
8. Vasiljevic, Z.Z.; Dojcinovic, M.P.; Jankovic-Castvan, I.; Ognjanovic, M.; Tadic, N.B.; Stojadinovic, S.; Brankovic, G.O.; Nokoloc, M.V. Photocatalytic degradation of methylene blue under natural sunlight using iron titanate nanoparticles prepared by a modified sol–gel method. *R. Soc. Open Sci.* **2020**, *7*, 200708. [CrossRef]
9. Tirumala, R.T.A.; Khatri, N.; Ramakrishnan, S.B.; Mohammadparast, F.; Khan, M.T.; Tan, S.; Wagle, P.; Puri, S.; McIlroy, D.N.; Kalkan, A.K.; et al. Tuning Catalytic Activity and Selectivity in Photocatalysis on Mie-Resonant Cuprous Oxide Particles: Distinguishing Electromagnetic Field Enhancement Effect from the Heating Effect. *ACS Sustain. Chem. Eng.* **2023**, *11*, 15931–15940. [CrossRef]
10. Xu, W.; Jain, P.K.; Beberwyck, B.J.; Alivisatos, A.P. Probing Redox Photocatalysis of Trapped Electrons and Holes on Single Sb-doped Titania Nanorod Surfaces. *J. Am. Chem. Soc.* **2012**, *134*, 3946–3949. [CrossRef]
11. Toloman, D.; Popa, A.; Stefan, M.; Pana, O.; Silipas, T.D.; Macavei, S.; Barbu-Tudoran, L. Impact of Gd ions from the lattice of TiO_2 nanoparticles on the formation of reactive oxygen species during the degradation of RhB under visible light irradiation. *Mater. Sci. Semicond. Process.* **2017**, *71*, 61–68. [CrossRef]
12. Toloman, D.; Mesaros, A.; Popa, A.; Silipas, T.D.; Neamtu, S.; Katona, G. V-doped ZnO particles: Synthesis, structural, optical and photocatalytic properties. *J. Mater. Sci. Mater. Electron.* **2016**, *27*, 5691–5698. [CrossRef]
13. Toloman, D.; Popa, A.; Stefan, M.; Silipas, T.D.; Suciu, R.C.; Barbu-Tudoran, L.; Pana, O. Enhanced photocatalytic activity of Co doped SnO_2 nanoparticles by controlling the oxygen vacancy states. *Opt. Mater.* **2020**, *110*, 110472. [CrossRef]
14. Ma, R.; Zhang, S.; Wen, T.; Gu, P.; Li, L.; Zhao, G.; Niu, F.; Huang, Q.; Tang, Z.; Wang, X. A critical review on visible-light-response CeO_2-based photocatalysts with enhanced photooxidation of organic pollutants. *Catal. Today* **2019**, *335*, 20–30. [CrossRef]
15. Banavar, S.; Deshpande, A.; Sur, S.; Andreescu, S. Ceria nanoparticle theranostics: Harnessing antioxidant properties in biomedicine and beyond. *J. Phys. Mater.* **2021**, *4*, 042003. [CrossRef]
16. Rashid, S.; Zaman, Z.; Nasir, M.; Ahmed, A.; Andreescu, S.; Liaquat, M.; Hayat, A. Nanoceria surface: The most sensitive redox-triggered one step nano-amplifier for fluorescence signal of ochratoxin A. *J. Nanostructure Chem.* **2022**, *12*, 223–233. [CrossRef]
17. Othman, A.; Hayat, A.; Andreescu, S. Eu-doped ceria nanocrystals as nanoenzyme fluorescent probes for biosensing. *Appl. Nano Mater.* **2018**, *1*, 5722–5735. [CrossRef]
18. Gubernatorova, E.O.; Liu, X.; Othman, A.; Muraoka, W.T.; Koroleva, E.; Andreescu, S.; Tumanov, A.V. Europium-doped cerium oxide nanoparticles limit reactive oxygen species formation and ameliorate intestinal ischemia–reperfusion injury. *Adv. Healthc. Mater.* **2017**, *6*, 1700176. [CrossRef]
19. Pansambal, S.; Oza, R.; Borgave, S.; Chauhan, A.; Bardapurkar, P.; Vyas, S.; Ghotekar, S. Bioengineered cerium oxide (CeO_2) nanoparticles and their diverse applications: A review. *Appl. Nanosci.* **2023**, *13*, 6067–6092. [CrossRef]
20. Saule, T.X.T.; Molinari, M.; Das, S.; Bhatta, U.M.; Mobus, G.; Parker, S.C.; Seal, S.; Sayle, D.C. Environment-mediated structure, surface redox activity and reactivity of ceria nanoparticles. *Nanoscale* **2013**, *5*, 6063–6073. [CrossRef]
21. Leel, N.S.; Kiran, M.; Kumawat, M.K.; Alvi, P.A.; Vats, V.S.; Patidar, D.; Dalela, B.; Kumar, S.; Dalela, S. Oxygen vacancy driven luminescence, ferromagnetic and electronic structure properties of Eu doped CeO_2 nanoparticles. *J. Lumin.* **2023**, *263*, 119981. [CrossRef]
22. Yang, H.; Xu, B.; Zhang, Q.; Yuan, S.; Zhang, Z.; Liu, Y.; Nan, Z.; Zhang, M.; Ohno, T. Boosting visible-light-driven photocatalytic performance of waxberry-like CeO_2 by samarium doping and silver QDs anchoring. *Appl. Catal. B* **2021**, *286*, 119845. [CrossRef]
23. Kumar, M.P.; Suganya Josephine, G.A.; Sivasamy, A. Oxidation of organic dye using nanocrystalline rare earth metal ion doped CeO_2 under UV and Visible light irradiations. *J. Mol. Liq.* **2017**, *242*, 789–797. [CrossRef]
24. Singh, K.; Kumar, K.; Srivastava, S.; Chowdhury, A. Effect of rare-earth doping in CeO_2 matrix: Correlations with structure, catalytic and visible light photocatalytic properties. *Ceram. Int.* **2017**, *43*, 17041–17047. [CrossRef]
25. Vinodkumar, T.; Rao, B.G.; Reddy, B.M. Influence of isovalent and aliovalent dopants on the reactivity of cerium oxide for catalytic applications. *Catal. Today* **2015**, *253*, 57–64. [CrossRef]
26. Trovarelli, A. Structural and oxygen storage/release properties of CeO_2-based solid solutions. *Comments Inorg. Chem.* **1999**, *20*, 263–284. [CrossRef]
27. Tang, Y.; Zhang, H.; Cui, L.; Ouyang, C.; Shi, S.; Tang, W.; Li, T.; Lee, J.S.; Chen, L. First-principles investigation on redox properties of M-doped CeO_2 (M = Mn, Pr, Sn, Zr). *Phys. Rev. B* **2010**, *82*, 125104. [CrossRef]
28. Reddy, B.M.; Katta, L.; Thrimurthulu, G. Novel nanocrystalline $Ce_{1-x}La_xO_{2-\delta}$ (x = 0.2) solid solutions: Structural characteristics and catalytic performance. *Chem. Mater.* **2010**, *22*, 467–475. [CrossRef]

29. Reddy, B.M.; Thrimurthulu, G.; Katta, L.; Yamada, Y.; Park, S.E. Structural characteristics, and catalytic activity of nanocrystalline ceria-praseodymia solid solutions. *J. Phys. Chem. C* **2009**, *113*, 15882–15890. [CrossRef]
30. Wang, Z.; Quan, Z.; Lin, J. Remarkable changes in the optical properties of CeO_2 nanocrystals induced by lanthanide ions doping. *Inorg. Chem.* **2007**, *46*, 5237–5242. [CrossRef]
31. Ramjeyanthi, N.; Alagar, M.; Muthuraman, D. Synthesis, structural and optical behavior of cerium oxide nanoparticles by co-precipitation method. *Int. J. Sci. Res. Sci. Tech.* **2018**, *4*, 44–51. [CrossRef]
32. Phokha, S.; Pinitsoontorn, S.; Chirawatkul, P.; Poo-arporn, Y.; Maensiri, S. Synthesis, characterization, and magnetic properties of monodisperse CeO_2 nanospheres prepared by PVP-assisted hydrothermal method. *Nanoscale Res. Lett.* **2012**, *7*, 425. [CrossRef] [PubMed]
33. Marabelli, F.; Wachter, P. Covalent insulator CeO_2: Optical reflectivity measurements. *Phys. Rev. B* **1987**, *36*, 1238–1243. [CrossRef] [PubMed]
34. Li, F.; Yu, X.H.; Pan, H.J.; Wang, M.L.; Xin, X.Q. Syntheses of MO_2 (M = Si, Ce, Sn) nanoparticles by solid-state reactions at ambient temperature. *Solid State Sci.* **2000**, *2*, 767–772. [CrossRef]
35. Derevyannikova, E.A.; Kardash, T.Y.; Kibis, L.S.; Slavinskaya, E.M.; Svetlichnyi, V.A.; Stonkus, O.A.; Ivanova, S.; Boronin, A.I. The structure and catalytic properties of Rh-doped CeO_2 catalysts. *Phys. Chem. Chem. Phys.* **2017**, *19*, 31883–31897. [CrossRef] [PubMed]
36. Zheng, H.; Hong, Y.; Xu, J.; Xue, B.; Li, Y.-X. Transesterification of ethylene carbonate to dimethyl carbonate catalyzed by CeO_2 materials with various morphologies. *Catal. Commun.* **2018**, *106*, 6–10. [CrossRef]
37. Si, R.; Zhang, Y.W.; You, L.P.; Yan, C.H. Rare-Earth Oxide Nanopolyhedra, Nanoplates, and Nanodisks. *Angew. Chem.* **2005**, *44*, 3256. [CrossRef]
38. Phuruangrat, A.; Thongtem, S.; Thongtem, T. Microwave-assisted hydrothermal synthesis and characterization of CeO_2 nanowires for using as a photocatalytic material. *Mater. Lett.* **2017**, *196*, 61–63. [CrossRef]
39. Santiago, A.A.G.; Andrade Neto, N.F.; Longo, E.; Paskocimas, C.A.; Motta, F.V.; Bomio, M.R.D. Fast and continuous obtaining of Eu^{3+} doped CeO_2 microspheres by ultrasonic spray pyrolysis: Characterization and photocatalytic activity. *J. Mater. Sci. Mater. Electron.* **2019**, *30*, 11508–11519. [CrossRef]
40. Yin, L.X.; Wang, Y.Q.; Pang, G.S.; Koltypin, Y.; Gedanken, A.J. Sonochemical syntesis of cerium oxide nanoparticles—Effect of additives and quantum size effect. *Colloid Interface Sci.* **2002**, *246*, 78–84. [CrossRef]
41. Bakkiyaraj, R.; Bharath, G.; Hasini Ramsait, K.; Abdel-Wahab, A.; Alsharaeh, E.H.; Chen, S.M.; Balakrishnan, M. Solution combustion synthesis and physico-chemical properties of ultrafine CeO_2 nanoparticles and their photocatalytic activity. *RSC Adv.* **2016**, *6*, 51238–51245. [CrossRef]
42. Amoresi, R.A.C.; Oliveira, R.C.; Marana, N.L.; De Almeida, P.B.; Prata, P.S.; Zaghete, M.A.; Longo, E.; Sambrano, J.R.; Simoes, A.Z. CeO_2 nanoparticle morphologies and their corresponding crystalline planes for the photocatalytic degradation of organic pollutants. *ACS Appl. Nano Mater.* **2019**, *2*, 6513–6526. [CrossRef]
43. Ortega, P.P.; Amoresi, R.A.C.; Teodoro, M.D.; Longo, E.; Ponce, M.A.; Simoes, A.Z. Relationship among morphology, photoluminescence emission, and photocatalytic activity of Eu-doped ceria nanostructures: A surface-type effect. *Ceram. Int.* **2023**, *49*, 21411–21421. [CrossRef]
44. Suciu, C.; Hoffmann, A.C.; Vik, A.; Goga, F. Effect of calcination conditions and precursor proportions on the properties of YSZ nanoparticles obtained by modified sol–gel route. *Chem. Eng. J.* **2008**, *138*, 608–615. [CrossRef]
45. Scherrer, P. Estimation of the size and structure of colloidal particles by Röentgen rays. *Nach. Ges. Wiss. Gottingen* **1918**, 98–100.
46. Laugier, J.; Bochu, B. *CELREF V3, Developed at the Laboratoire des Matériaux et du Génie Physique*; Ecole Nationale Supérieure de Physique de Grenoble (INPG): Grenoble, France, 2003.
47. Stefan, M.; Leostean, C.; Pana, O.; Toloman, D.; Popa, A.; Perhaita, I.; Senila, M.; Marincas, O.; Barbu-Tudoran, L. Magnetic recoverable Fe_3O_4-TiO_2:Eu composite nanoparticles with enhanced photocatalytic activity. *Appl. Surf. Sci.* **2016**, *390*, 248–259. [CrossRef]
48. Chiang, T.L.; Wang, Y.C.; Ding, W.H. Trace determination of rhodamine B and rhodamine 6G dyes in aqueous samples by solid-phase extraction and high-performance liquid chromatography coupled with fluorescence detection. *J. Chin. Chem. Soc.* **2012**, *59*, 515–519. [CrossRef]
49. Yang, N.; Orgiani, P.; Di Bartolomeo, E.; Foglietti, V.; Torelli, P.; Ievlev, A.V.; Rossi, G.; Licoccia, S.; Balestrino, G.; Kalinin, S.V.; et al. Effects of dopant ionic radius on cerium reduction in epitaxial cerium oxide thin films. *J. Phys. Chem. C* **2017**, *121*, 8841–8849. [CrossRef]
50. Hong, S.J.; Virkar, A.V. Lattice parameters and densities of rare-earth oxide doped ceria electrolytes. *J. Am. Ceram. Soc.* **1995**, *78*, 433–439. [CrossRef]
51. Shannon, R.D.; Prewitt, C.T. Effective ionic radii in oxides and fluorides. *Acta Crystallogr. Sect. B Struct. Crystallogr. Cryst. Chem.* **1969**, *25*, 925–946. [CrossRef]
52. Shannon, R.D. Revised Effective Ionic Radii and Systematic Studies of Interatomic Distances in Halides and Chalcogenides. *Acta Cryst.* **1976**, *32*, 751–767. [CrossRef]
53. Goharshadia, E.K.; Samiee, S.; Nancarrow, P. Fabrication of cerium oxide nanoparticles: Characterization and optical properties. *J. Colloid Interface Sci.* **2011**, *356*, 473–480. [CrossRef] [PubMed]

54. Deus, R.C.; Cortés, J.A.; Ramirez, M.A.; Ponce, M.A.; Andres, J.; Rocha, L.S.R.; Longo, E.; Simões, A.Z. Photoluminescence properties of cerium oxide nanoparticles as a function of lanthanum content. *Mater. Res. Bull.* **2015**, *70*, 416–423. [CrossRef]
55. Sun, C.; Li, H.; Zhang, H.; Wang, Z.; Chen, L. Controlled synthesis of CeO_2 nanorods by a solvothermal method. *Nanotechnology* **2005**, *16*, 1454–1463. [CrossRef]
56. Liu, X.; Chen, S.; Wang, X. Synthesis and photoluminescence of CeO_2:Eu^{3+} phosphor powders. *J. Lumin.* **2007**, *127*, 650–654. [CrossRef]
57. Singh, M.; Goyal, M.; Devlal, K. Size and shape effects on the band gap of semiconductor compound nanomaterials. *J. Taibah Univ. Sci.* **2018**, *12*, 470–475. [CrossRef]
58. Binnemans, K. Interpretation of europium(III) spectra. *Coord. Chem. Rev.* **2015**, *295*, 1–45. [CrossRef]
59. Li, L.; Yang, H.K.; Moon, B.K.; Fu, Z.; Guo, C.; Jeong, J.H.; Yi, S.S.; Jang, K.; Lee, H.S. Photoluminescence properties of CeO_2:Eu^{3+} nanoparticles synthesized by a sol-gel method. *J. Phys. Chem. C* **2009**, *113*, 610–617. [CrossRef]
60. Vimal, G.; Mani, K.P.; Biju, P.R.; Joseph, C.; Unnikrishnan, N.V.; Ittyachen, M.A. Structural studies and luminescence properties of CeO_2:Eu^{3+} nanophosphors synthesized by oxalate precursor method. *Appl. Nanosci.* **2015**, *5*, 837–846. [CrossRef]
61. Hernández-Alonso, M.D.; Hungria, A.B.; Martinez-Arias, A.; Fernández-Garcia, M.; Coronado, J.M.; Carlos Conesa, J.; Soria, J. EPR study of the photoassisted formation of radicals on CeO_2 nanoparticles employed for toluene photooxidation. *Appl. Catal. B Environ.* **2004**, *50*, 167–175. [CrossRef]
62. Oliva, C.; Termignone, G.; Vatti, F.P.; Forni, L.; Vishniakov, A.V. Electron paramagnetic resonance spectra of CeO_2 catalyst for CO oxidation. *J. Mater. Sci.* **1996**, *31*, 6333–6338. [CrossRef]
63. Soria, J.; Conesa, J.C.; Martinez-Arias, A. Characterization of surface defects in CeO_2 modified by incorporation of precious metals from chloride salts precursors: An EPR study using oxygen as probe molecule. *Colloids Surf. A Physicochem. Eng. Asp.* **1999**, *158*, 67–74. [CrossRef]
64. Cerrato, E.; Gionco, C.; Paganini, M.C.; Giamello, E.; Albanese, E.; Pacchioni, G. Origin of visible light photoactivity of the CeO_2/ZnO heterojunction. *ACS Appl. Energy Mater.* **2018**, *1*, 4247–4260. [CrossRef]
65. Li, Y.F.; Zhang, W.P.; Li, X.; Yu, Y. TiO_2 nanoparticles with high ability for selective adsorption and photodegradation of textile dyes under visible light by feasible preparation. *J. Phys. Chem. Solids.* **2014**, *75*, 86–93. [CrossRef]
66. Brezova, V.; Gabcova, S.; Dvoranova, D.; Stasko, A. Reactive oxygen species produced upon photoexcitation of sunscreens containing titanium dioxide (an EPR study). *J. Photochem. Photobiol. B* **2005**, *79*, 121–134. [CrossRef] [PubMed]
67. Lázaro-Martínez, M.; Leal-Denis, M.F.; Piehl, L.L.; Rubín de Celis, E.; Buldain, G.Y.; Dall'-Orto, V.C. Studies on the activation of hydrogen peroxide for color removal in the presence of a new Cu(II)-polyampholyte heterogeneous catalyst. *Appl. Catal. B Environ.* **2008**, *82*, 273–283. [CrossRef]
68. Yang, Z.; Xu, M.; Liu, Y.; He, F.; Gao, F.; Su, Y.; Wei, H.; Zhang, Y. Nitrogen-doped, carbon-rich, highly photoluminescent carbon dots from ammonium citrate. *Nanoscale* **2014**, *6*, 1890–1895. [CrossRef]
69. Veedu, S.N.; Jose, S.; Narendranath, S.B.; Kurup, M.R.P.; Periyat, P. Visible light-driven photocatalytic degradation of methylene blue dye over bismuth-doped cerium oxide mesoporous nanoparticles. *Environ. Sci. Pollut. Res.* **2021**, *28*, 4147–4155. [CrossRef]